Mechanism of Selective and Complete Oxidation in La2O3-catalyzed Oxidative Coupling of Methane Reaction

ARTICLE

Mechanism of Selective and Complete Oxidation in La$_2$O$_3$-catalyzed Oxidative Coupling of Methane Reaction†

Shibin Wang,[a,b,c] Shenggang Li*[a,b] and David A. Dixon*[d]

Periodic density function theory (DFT) calculations were performed to study the evolution of surface oxygen species on the La$_2$O$_3$ catalyst during the oxidative coupling of methane (OCM) reaction, and to establish the catalytic mechanism of the selective and complete oxidation of CH$_4$. The lattice oxygen (O^{2-}) site on the stoichiometric La$_2$O$_3$ surface activates CH$_4$ via heterolytic C−H bond cleavage to yield CH$_3^-$ and H$^+$ fragments, which bind to surface Lewis acid (La^{3+}) and Brönsted base (O^{2-}) sites, respectively. In the presence of the H$^+$ fragment, the CH$_3^-$ fragment binds quite strongly to the above La$_2$O$_3$ surface, but O$_2$ adsorption facilitates its desorption as a gaseous CH$_3$ radical at relatively low reaction temperatures, while molecular O$_2$ adsorbed at the La^{3+} site becomes a superoxo radical (O$_2^{\bullet-}$) species. This O$_2^{\bullet-}$ species reacts with a second CH$_4$ molecule via direct H abstraction to produce another gaseous CH$_3$ radical, accompanied by its transformation into a hydrogenperoxo (HO$_2^-$) species, which transfers an O atom to a neighboring O^{2-} site and converts the latter into a peroxo (O$_2^{2-}$) site. Whereas CH$_4$ activation at the O^{2-} site is essentially an acid-base reaction, that at the O$_2^{2-}$ site is clearly a redox reaction, which occurs via an O insertion mechanism to directly form gaseous CH$_3$OH as further confirmed by our ab initio molecular dynamics (AIMD) calculations. CH$_3$OH is further oxidized by additional O$_2^{2-}$ site to yield CO$_2$ following a similar mechanism, whereas CO may form from dehydrogenatio of the CH$_2$O intermediate at the same site. Thus, the O$_2^{2-}$ site is proposed to be responsible for complete oxidation of CH$_4$ in the OCM reaction, whereas the O^{2-} and O$_2^{\bullet-}$ sites are responsible for the formation of gaseous CH$_3$ radicals and thus C$_2$ products. Our proposed catalytic mechanism is based on first principles DFT calculations, which gives a comprehensive view of CH$_4$ interaction with the different oxygen species on the La$_2$O$_3$ catalyst surface, and provides critical insights into the possible evolution of surface oxygen species and the detailed surface reaction network.

Introduction

Due to the increasing exploration and utilization of unconventional natural gas, the efficient conversion of CH$_4$ into value−added chemicals such as C$_2$H$_4$ by the oxidative coupling of methane (OCM) reaction is of growing importance.[1–3] It is generally accepted that C$_2$ products (C$_2$H$_6$ and C$_2$H$_4$) result from direct coupling of CH$_3$ radicals in the gas phase, which are formed by CH$_4$ activation at oxygen sites on the catalyst surface.[4–6] Highly reactive catalysts are required to catalyze the OCM reaction due to the high C−H bond energy in CH$_4$; however, an issue is that the resulting CH$_3$ radicals or C$_2$ products are more reactive and thus can be easily oxidized to generate CO and CO$_2$ byproducts, as the over-oxidation reactions are thermodynamically and, possibly also kinetically, favorable. Thus, the challenge for continued catalyst development lies in balancing reactivity with selectivity.[7] Over the past three decades, a large number of catalysts, such as doped alkali metal oxides (Li/MgO),[8,9] doped rare earth metal oxides (Sr/La$_2$O$_3$),[10] and mixed transition metal oxides (Mn−Na$_2$WO$_4$/SiO$_2$)[11–14] were extensively investigated for optimizing the C$_2$ yield in the OCM reaction. Among the known OCM catalysts, La$_2$O$_3$ catalysts exhibit good activity but relatively low C$_2$ yields, and the relatively low operational temperature may give the La$_2$O$_3$ catalyst a great advantage.[15–18] For examples, Jiang et al prepared La$_2$O$_3$ catalysts of different dimensionalities, yielding CH$_4$ conversion and C$_2$ selectivity up to 32% and 46%, respectively, with the reaction temperature of 823 K.[19]

To limit the extent of over-oxidation and to improve C$_2$ selectivity, a lower amount of O$_2$ is usually used in the reaction stream, resulting in limited CH$_4$ conversion with usually complete O$_2$ consumption.[20] In addition, the most efficient OCM catalysts such as Li/MgO and Sr/La$_2$O$_3$ are oxide materials with strong basicity and little oxidation capability, so oxidation may be mostly attributed to gaseous O$_2$. Indeed, isotope-labelled experiments under OCM conditions and corresponding computational studies reveal the occurrence of O$_2$ dissociative adsorption over the La$_2$O$_3$ surface to generate active oxygen species.[21,22] We have previously investigated O$_2$ chemisorption over low−index La$_2$O$_3$ surfaces, and peroxo (O$_2^{2-}$) sites were predicted to form upon O$_2$ dissociation.[23] O$_2$ dissociation over the stoichiometric La$_2$O$_3$ (001) surface was predicted to be modestly endothermic (64.6 kJ mol^{-1}) with a sizable energy barrier (124.5 kJ mol^{-1}) at 0 K. Nevertheless, the nature of the active oxygen species and its evolution, and the detailed catalytic mechanism of the OCM reaction remain elusive.

[a.] CAS Key Laboratory of Low−Carbon Conversion Science and Engineering, Shanghai Advanced Research Institute, Chinese Academy of Sciences, 100 Haike Road, Pudong District, Shanghai 201203, China. E-mail: lisg@sari.ac.cn.
[b.] School of Physical Science and Technology, ShanghaiTech University, 393 Middle Huaxia Road, Pudong District, Shanghai 201203, China.
[c.] Department of Chemistry and Key Laboratory of Organic Optoelectronics & Molecular Engineering of Ministry of Education, Tsinghua University.
[d.] Department of Chemistry and Biochemistry, The University of Alabama, Shelby Hall, Box 870336, Tuscaloosa, Alabama 35487-0336, United States. E-mail: dadixon@ua.edu.

Numerous experiments have been carried out to elucidate the role of surface oxygen species in the OCM reaction.[24] The activated forms of the surface oxygen species in the OCM reaction may include lattice oxygen (O^{2-}), peroxo (O_2^{2-}), superoxo radical ($O_2^{\bullet-}$), and oxygen radical ($O^{\bullet-}$). For the Li/MgO catalyst, Discoll et al. proposed the $O^{\bullet-}$ site near the Li^+ dopant to be responsible for CH_4 activation,[25] although for La_2O_3 and other rare earth metal oxide-based OCM catalysts, there is a lack of direct experimental evidence for the presence of the $O^{\bullet-}$ site. In situ Raman spectroscopy was employed by Lunsford et al. to demonstrate the presence of the O_2^{2-} site on the Ba/MgO catalyst,[26] and X-ray photoelectron spectroscopy (XPS) studies on the same catalyst showed a correlation between the catalytic activity and near−surface O_2^{2-} concentration.[27] Furthermore, Wang et al. detected the $O_2^{\bullet-}$ species on the La_2O_3 catalyst surface using electron paramagnetic resonance (EPR) spectroscopy.[28] However, Louis et al. raised doubt about the stability of the $O_2^{\bullet-}$ species on the La_2O_3 surface under OCM conditions on the basis of the low oxygen partial pressure commonly used in the reaction.[29] Xu et al detected surface superoxide (O_2^-) species over the $La_2B_2O_7$ (B= Ti^{4+}, Zr^{4+}, Ce^{4+}) catalysts, and suggested the important role of this species in determining the OCM activity, where the $La_2Ce_2O_7$ catalyst with the highest amount of O_2^- sites exhibited the highest reactivity.[30] Thus, most of the above-mentioned surface oxygen sites are likely to be present on the La_2O_3 catalyst surface during the OCM reaction, and it is of great interest to reveal the role and the evolution of these surface oxygen species.

First principles-based electronic structure calculations have also been performed to investigate CH_4 activation at different surface oxygen sites. Density functional theory (DFT) calculations were performed by Palmer et al. to examine CH_4 activation by surface O^{2-}, O_2^{2-}, and $O^{\bullet-}$ species on the La_2O_3(001) surface.[31] Direct hydrogen abstraction from CH_4 by O^{2-} on the stoichiometric La_2O_3 (001) slab surface was predicted to be very endothermic at 383.0 kJ mol^{-1}, whereas that by $O^{\bullet-}$ on the nonstoichiometric $La_2O_{3.33}$ (001) slab surface was calculated to be exothermic with a very low energy barrier of 42.5 kJ mol^{-1}. The energy barrier for the reaction of CH_4 with the O_2^{2-} site was predicted to be quite high at 197.8 kJ mol^{-1}. Wang et al. recently proposed two strategies to improve the reactivity of the La_2O_3 catalyst: constructing surfaces with low coordination number oxygen sites, e.g. the La_2O_3 (210) surface, and doping the La_2O_3 (001) surface with Sr or Ce. The energy barriers of CH_4 dissociation were calculated at the PBE level to be 86.8, 113.9, and 135.1 kJ mol^{-1} for the La_2O_3 (210), Sr-doped La_2O_3 (001), and Ce-doped La_2O_3 (001) surfaces, respectively.[32] We have previously investigated the mechanism of CH_4 activation at the O_2^{2-} site using La_2O_3 cluster models.[33] In addition to the hydrogen abstraction mechanism found on very small clusters with well-exposed O_2^{2-} sites, on larger clusters with less-exposed O_2^{2-} sites, we predicted that the O_2^{2-} site activates CH_4 by directly inserting an O atom into the CH_3−H bond. CH_3OH is produced in this process, and the reaction is highly exothermic but with a considerable energy barrier. With the La_4O_7 (C_{2v}) cluster model, the exothermicity and energy barrier were calculated to be −180.3 kJ mol^{-1} and 180.7 kJ mol^{-1}, respectively. In addition, Chrétien and Metiu carried out DFT calculations to study CH_4 dissociation at the O^{2-} site on the stoichiometric La_2O_3 (001) surface, and the resulting CH_3^- and H^+ fragments were predicted to preferentially adsorb at the La^{3+} and O^{2-} sites, respectively; this was attributed to an acid−base interaction, although the energy barrier for this process was not reported.[34] Using stoichiometric La_2O_3 cluster models, we previously investigated CH_4 activation at the La^{3+}−O^{2-} pair site at the DFT and coupled cluster (CCSD(T)) levels of theory.[35] The energy barriers (ΔE_{0K}) from the physisorption state were predicted to be modest at ~104.2 kJ mol^{-1}. Furthermore, we were able to establish a linear relationship between the acid−base properties of the La^{3+}−O^{2-} pair site in

terms of the CO_2 chemisorption energy and its reactivity with CH_4.[36] Regarding the role of gaseous O_2 in the OCM reaction catalyzed by oxides with strong basicity such as MgO, Schwach et al. suggested that gaseous O_2 might merely act as an electron acceptor to facilitate the formation of the CH_3 radical, and proposed that the $O_2^{\bullet-}$ radical species generated in this process was adsorbed on the MgO surface near a proton.[37] However, molecular level understanding of this process and of the detailed catalytic mechanism of the OCM reaction in general remains lacking.

In this work, we used the symmetric and stoichiometric low−index La_2O_3(001) surface as a model for the La_2O_3 catalyst, and we performed periodic DFT calculations to study the catalytic mechanism of the OCM reaction. Gibbs free energy surfaces at the relevant reaction temperature of 823 K were predicted to fully elucidate the catalytic mechanisms under realistic reaction conditions, and the evolution of the surface oxygen species was also revealed. Our computational studies provide critical insights into the role of the surface oxygen species and the detailed catalytic reaction network for selective and complete CH_4 oxidation.

Results and discussion

CH_4 Selective Oxidation.

The stoichiometric La_2O_3(001) slab model and the computational method used in this work are similar to our previous work,[23] although we now consider a number of additional factors affecting the accuracy of our results, which are mostly discussed in the Computational section. The Gibbs free energy surface for CH_4 activation at the O^{2-} site on the La_2O_3(001) slab surface at the relevant reaction temperature of 823 K is shown in Figure 1(a). Physisorption of CH_4 on the La_2O_3(001) surface is very weak, so CH_4 activation should occur without pre-adsorption and by direct collisions of the gaseous CH_4 molecule with the La_2O_3 surface at any relevant reaction temperature. A significant free energy barrier (G_a) of 269.2 kJ mol^{-1} was predicted for CH_4 dissociation, leading to the chemisorption structure with the CH_3^- fragment adsorbed at the bridge site between two adjacent La atoms (La_b) and with the H^+ fragment adsorbed at the top site on the O atom (O_t). We note that the energy barrier at 0 K (E_a) is considerably lower at 161.9 kJ mol^{-1}, but the temperature-dependent pre-exponential factor should be very low for such as a direct-collision-induced gas-surface reaction. Thus, CH_4 dissociation at the O^{2-} site involves two neighboring La^{3+} sites, leading to heterolytic CH_3−H bond splitting to yield the CH_3^- and H^+ fragments, which bind to the Lewis acid (La_b) and Brönsted base (O_t) sites, respectively, consistent with previous studies.[34-36] For this reason, the La^{3+} and O^{2-} sites are labelled separately with La* and O* in all figures, and the CH_3^- and H^+ species adsorbed at these sites are denoted as CH_3−La* and H−O*, respectively. Bader charge analysis[38–40] shows that the CH_3^- and H^+ fragments carry negative and positive charges of −0.66 |e| and +0.61 |e| in the transition state, and −0.67 |e| and +0.59 |e| in the chemisorption state, respectively, confirming the heterolytic nature of the bond splitting. In addition, CH_4 dissociation clearly involves a late transition state due to the high endothermicity of 259.3 kJ mol^{-1}, and the average La−C and O−H distance in the transition state of 3.00 Å and 0.99 Å are very close to those in the chemisorption state of 2.86 Å and 0.97 Å. The proximity of

the transition state to the product chemisorption state makes it very difficult to locate this transition state.[31,34] Vibrational frequencies of the transition state were also calculated, and only one imaginary frequency of $143i$ cm^{-1} was predicted, which has the correct displacements (Figure S1), confirming it as the right transition state. This low frequency is consistent with the lateness of the transition state. In addition, in the presence of the H$^+$ adsorbate at the O$_t$ site, the CH$_3^-$ adsorbate binds quite strongly to the La$_b$ site, as the free energy of desorption as a CH$_3$ radical from the La$_b$ site was predicted to be 100.7 kJ mol^{-1}. As the direct desorption process is just an endothermic process without any transition state, the effective free energy barrier (G$_{a,eff}$) for CH$_4$ activation on the La$_2$O$_3$ (001) surface to directly form the CH$_3$ radical, defined as the free energy relative to the separated reactants (the stoichiometric surface and the CH$_4$ molecule), is thus 360.0 kJ mol^{-1}. At 0 K, the reaction energy for CH$_4$ dissociation on the La$_2$O$_3$ (001) surface to form the CH$_3$ radical was calculated to be 387.9 kJ mol^{-1}, and this value is only slightly larger than the previously calculated reaction energy of 383.0 kJ mol^{-1},[31] and is ~51.1 kJ mol^{-1} less than the first C-H bond dissociation energy (BDE) in CH$_4$ of 439.0 kJ mol^{-1}.[41]
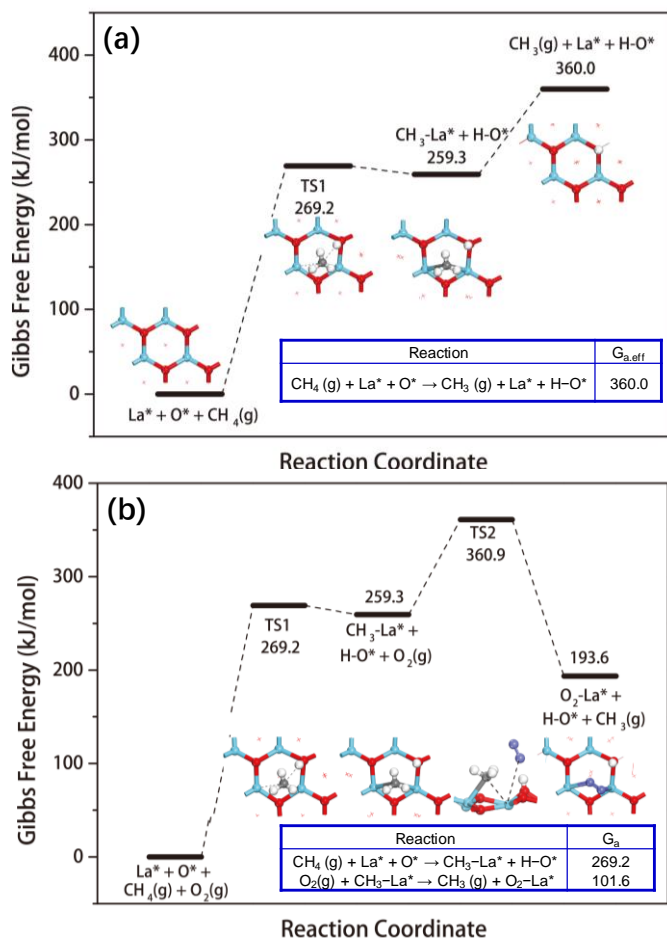
Figure 1. Calculated Gibbs free energy diagram (ΔG$_{823K}$, kJ mol^{-1}) for CH$_4$ dissociation at the O^{2-} site on the La$_2$O$_3$ (001) surface. (a) CH$_3$ direct desorption. (b) O$_2$−assisted CH$_3$ desorption. The La^{3+}−O^{2-} pair site is considered as a combination of the La^{3+} site (La*) and the neighbouring O^{2-} site (O*).

The above charge analysis suggests that an ionic interaction between the CH$_3^-$ adsorbate and the La site exists and contributes to the high desorption energy of the CH$_3$ radical from the La site, with E$_{des}$ of 232.6 kJ mol^{-1} at 0 K. This is confirmed by an electron localization function (ELF) analysis shown in Figure S2(a), which reveals that the electron density is highly localized around the C atom, and little electron density appears between the C—La bond, indicating that interaction between the CH$_3^-$ adsorbate and the La site is dominated by an ionic interaction instead of covalent bonding. This is further validated by crystal orbital Hamilton population (COHP) analysis shown in Figure S2(b), which reveals that there is no obvious covalent interaction in the bonding area between the C atom and the relevant La site. As also shown in the projected density of states (PDOS) plot in Figure S3, with the CH$_3^-$ adsorbate at the relevant La site, the frontier orbitals in the valence band and conduction band are dominated by the C 2p and La 5d orbitals, respectively. When the CH$_3$ radical desorbs from the La site, the CH$_3^-$ fragment must transfer an electron from its C 2p orbital to the La 5d orbital of the surface, and a high energy input is required for breaking the ionic interaction, which can be correlated with the estimated band gap of 278.8 kJ mol^{-1}, and contributes to the high desorption energy of the CH$_3$ radical from the La site.

As mentioned above, CH$_4$ physisorption on the La$_2$O$_3$ (001) surface is very weak, so it does not bind to the surface at any practical reaction temperature. Furthermore, the significant instability of the chemisorbed heterolytic pair relative to the separated reactants also makes it unlikely to be observed. As the direct release of the CH$_3$ radical while leaving an H atom on the catalyst surface requires a very high energy input, just slightly below the first BDE of CH$_4$, this process is not really catalytic. Upon desorption of the CH$_3$ radical from the surface, the extra electron from the CH$_3^-$ adsorbate returns to the surface, although the resulting slab model remains neutral due to the H$^+$ adsorbate. Spin-polarized calculation of the H−adsorbed surface shows that each of the four surface La atoms carries a magnetic moment of 0.04~0.05 μ_B (the spin magnetic moment of each unpaired electron is 1.0 μ_B, although the total magnetic moment of an atom also has contribution from its orbital magnetic moment). Bader charge analysis further shows that each of these surfaces La atoms carries a positive charge of +1.96 |e|. These values are to be compared with those of 0.0 μ_B and +2.02 |e|, respectively, for the stoichiometric surface, suggesting that the surface La sites on the H-adsorbed surface are only slightly reduced upon electron transfer from the CH$_3^-$ adsorbate.

CH$_4$ reactivity of the H-adsorbed surface was also investigated, and the potential energy surface is shown in Figure S6. The free energy of the reaction at 823 K remains very positive at 231.1 kJ mol^{-1} with a high free energy barrier of 245.9 kJ mol^{-1}, although most of this barrier is due to the endothermicity, so the H-adsorbed La$_2$O$_3$(001) surface has similar CH$_4$ reactivity as the stoichiometric surface. Due to the fact that the formation of the H−adsorbed La$_2$O$_3$(001) surface requires significant energy input for CH$_4$ dissociation on the stoichiometric surface as shown in Figure 1(a), CH$_4$ reaction with the H−adsorbed surface was not further considered.

In addition, we examined alternative routes for the further evolution of the CH_4 chemisorption state on the stoichiometric La_2O_3(001) surface. First, as shown in Figure S7, the migration of the CH_3 species adsorbed at the La* site to another nearby O* site to form CH_3–O* was predicted to be highly endothermic by 264.4 kJ mol^{-1}, consistent with the previous prediction that the chemisorption state in Figure 1(a) is the most stable adsorption structure.[34] Second, we failed to locate a local minimum corresponding to the transfer of another H atom from the CH_3 species to a nearby O* site to form CH_2–La*, as the H atom was transferred back upon relaxation.

For the MgO-based OCM catalyst, molecular O_2 was proposed to facilitate the formation of the CH_3 radical, and the reaction energy for CH_4 dissociation to form the CH_3 radical was calculated to drop from 228.7 kJ mol^{-1} to 37.6 kJ mol^{-1} with the assistance of O_2.[42] Our calculations show that at relatively low temperatures, molecular O_2 can indeed promote the desorption of the CH_3 species from the CH_4 chemisorption state via competitive adsorption at the La_b site, and as shown in Figure S12(b), a surface superoxo ($O_2^{\bullet-}$) species forms at the La_b site upon the release of the CH_3 radical into the gas phase, which is exothermic by −49.2 kJ mol^{-1} with a negligible energy barrier of 4.8 kJ mol^{-1} at 0 K, suggesting that O_2-assisted CH_3 desorption is favorable both thermodynamically and kinetically. Bader charge analysis shows that the $O_2^{\bullet-}$ species carries a negative charge of −0.76 $|e|$, which is nearly half of that calculated for the lattice O^{2-} of −1.33 $|e|$, consistent with our formal charge assignment. However, the above reaction is again a gas-surface reaction without pre-adsorption of the gaseous reactant at any relevant reaction temperature, and should occur by direct collisions of the O_2 molecules with the surface. Thus, although the energy barrier at 0 K (E_a) is negligible, the pre-exponential factor can be expected to be very small, and the free energy barrier (G_a) is substantial at 101.6 kJ mol^{-1} at 823 K as shown in Figure 1 (b), despite the fact that the reaction remains exothermic by −65.7 kJ mol^{-1}. This free energy barrier is actually comparable with the free energy of direct desorption of the CH_3 radical (100.7 kJ mol^{-1}) shown in Figure 1 (a), suggesting that direct CH_3 desorption becomes competitive with the O_2-assisted route at 823 K, and further increasing (reducing) the reaction temperature will favor the direct (O_2-assisted) pathway. Furthermore, the O_2-assisted route obviously requires the presence of gaseous O_2, so the direct desorption pathway may dominate when gaseous O_2 is largely consumed even below 823 K. At 823 K, the effective free energy barrier for O_2-assisted CH_4 dissociation to form the CH_3 radical on the stoichiometric La_2O_3 (001) surface is 360.9 kJ mol^{-1}, comparable to that of the direct desorption route of 360.0 kJ mol^{-1}, consistent with the above conclusions on the temperature effect. We also note that our O_2-assisted CH_4 dissociation route is similar to some extent to that proposed by Cooper et al[43] for CH_4 activation over the yttrium-stabilized zirconia (YSZ) surface in the presence of O_2, where homolytic cleavage of the CH_3–H bond was suggested to occur with the electron from the H atom transferred to the O_2 molecule to also yield the $O_2^{\bullet-}$ species.

As discussed above, due to the significant instability of the CH_4 chemisorption state with respect to the separated reactants on the stoichiometric La_2O_3(001) surface, the coverage of the chemisorbed heterolytic pair can be expected to be very low. Nevertheless, the exothermicity from O_2 adsorption before or after CH_3 radical desorption can still play an important role in driving the reaction forward. For other La_2O_3 surfaces on which CH_4 chemisorption is exothermic, the coverage of the chemisorbed heterolytic pair can become appreciable especially at relatively low temperature.

Evolution of Surface Oxygen Species.

As shown in Figure 1(b), CH_4 dissociation at the La_b–O_t pair site followed by O_2-assisted CH_3 desorption or direct CH_3 desorption followed by O_2 adsorption leads to formation of the $O_2^{\bullet-}$ species at the La_b site along with the co-adsorbed H^+ species at the neighboring O_t site. The above pair site must be regenerated for the completion of the OCM catalytic cycle, and thus we further investigated the reactions of the $O_2^{\bullet-}$ species with CH_4.

The free energy diagram for the CH_4 reaction with the $O_2^{\bullet-}$ species is shown in Figure 2(a), which can be considered as a continuation from that in Figure 1(b). CH_4 first reacts with the $O_2^{\bullet-}$ species to yield the second CH_3 radical, which incurs a significant free energy barrier of 237.3 kJ mol^{-1} at 823 K, and the free energy of the reaction is 130.7 kJ mol^{-1}. This is again a gas-surface reaction without pre-adsorption of the gaseous reactant. Different from the CH_4 activation mechanism at the La_b–O_t pair site, the $O_2^{\bullet-}$ species directly abstracts an H atom from CH_4, leading to homolytic splitting of the C–H bond and the prompt release of the second CH_3 radical. Bader charge analysis shows that the total negative charges carried by the two O atoms are −0.76 $|e|$, −1.25 $|e|$, and −1.36 $|e|$ in the initial state, the transition state, and the final state, respectively. Magnetic moments of these two oxygen atoms were calculated to be 0.40 and 0.38 μ_B in the initial state, and zero in the final state. These are consistent with the conversion of the $O_2^{\bullet-}$ species to the hydrogenperoxo (HO_2^-) species upon CH_4 activation. Comparing the effective energy barrier for CH_3 radical formation at the O^{2-} site (360.0 or 360.9 kJ mol^{-1}) shown in Figure 1 and that involving the O_2^- species (237.3 kJ mol^{-1}) shown in Figure 2(a), we conclude that the $O_2^{\bullet-}$ site on the La_2O_3(001) surface is more reactive than the O^{2-} site with CH_4.

The HO_2^- species can be considered as a precursor of hydrogen peroxide (H_2O_2), which is thermodynamically unstable at OCM conditions, so we consider its further evolution via another reaction channel. As also shown in Figure 2(a), the HO_2^- species adsorbed at the La_b site readily reacts with a neighboring lattice O^{2-} site to yield a hydroxide (OH$^-$) species adsorbed at the La^{3+} top site (La_t), which is accompanied by the conversion of the lattice O^{2-} site to a peroxo (O_2^{2-}) site. The latter is written as O–O* to signify its connection with the lattice O^{2-} site, although the exposed O atom also interacts with two neighboring La^{3+} sites. This process is exothermic by −68.2 kJ mol^{-1} with a very low energy barrier of 26.6 kJ mol^{-1}. Bader charge analysis shows that the O_2^{2-} site carries the total negative charge of −1.38 $|e|$, which is very close to that at the lattice O^{2-} site of −1.33 $|e|$. Furthermore, similar to the case of the HO_2^- species adsorbed at the La_b site, the two oxygen atoms at the O_2^{2-} site were predicted to have zero magnetic moments. These are consistent with our assignment.

The O_2^{2-} site can further react with CH_4, and we have previously found that CH_4 can be activated by direct insertion of an exposed O atom from the O_2^{2-} site on the $La_{2n}O_{3n+1}$ clusters into the CH_3-H bond to produce CH_3OH.[33] A similar reaction mechanism is proposed for the O_2^{2-} site on the La_2O_3 (001) surface, and the free energy surface for CH_4 activation at the
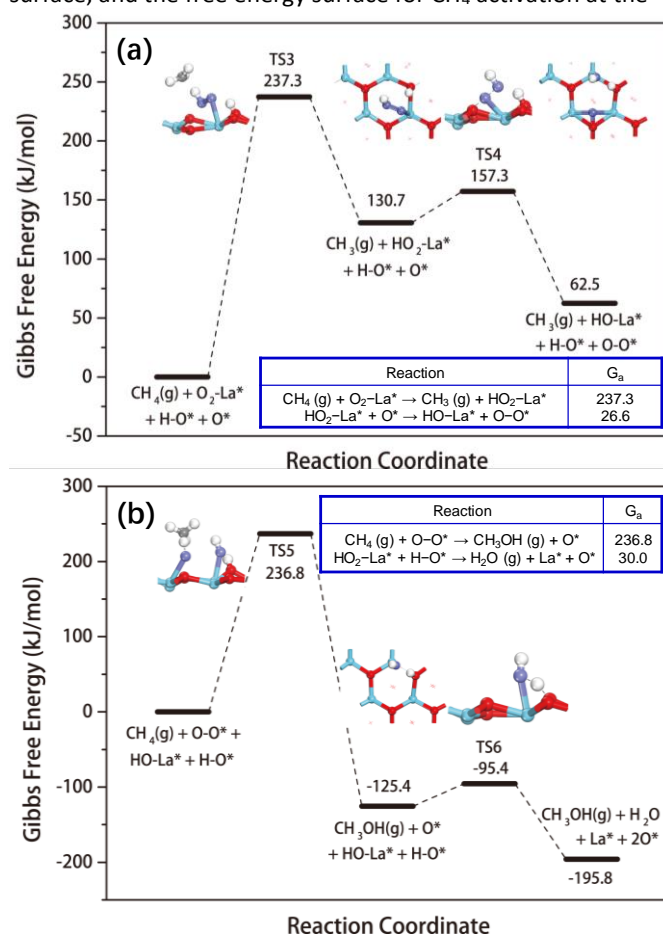
Figure 2. Calculated Gibbs free energy diagram (ΔG_{823K}, kJ mol^{-1}) for CH_4 activation by the $O_2^{\bullet-}$ species and at the O_2^{2-} site on the La_2O_3(001) surface, which continues from that on Figure 1(b). (a) CH_3 direct formation by reacting with the $O_2^{\bullet-}$ species. (b) CH_3OH direct formation at the O_2^{2-} site.

O_2^{2-} site on the La_2O_3(001) surface is shown in Figure 2(b). CH_4 is oxidized by the O_2^{2-} site to form CH_3OH, which is very exothermic at -125.4 kJ mol^{-1}, although it has a relatively free energy barrier (236.8 kJ mol^{-1}) at 823 K. We note that this is once again a gas-surface reaction without pre-adsorption of the gaseous reactant at any relevant reaction temperature. The $O-C$ and $O-H$ distances in the transition state are 2.21 and 1.10 Å, respectively. Vibrational frequencies of this transition state were calculated, and only one imaginary frequency of 745i cm^{-1} was found. As shown by the vector displacement of the imaginary frequency (Figure S1), the exposed O atom from the O_2^{2-} site moves towards the C atom, while the H atom from CH_4 moves toward the O atom, consistent with the formation of CH_3OH.

To further verify the formation of CH_3OH at the O_2^{2-} site, we performed ab initio molecular dynamics (AIMD) simulations

starting from the transition state structure, and to simplify the AIMD simulations, we removed both the H adsorbate at the O_t site and the OH adsorbate at the La_t site, which would further combine and desorb as an H_2O molecule as discussed below. The potential energy surface is shown in Figure S4, and the transition state has a comparable imaginary frequency of 731i cm^{-1}. Our AIMD simulations show that at ~37 fs, the H atom was transferred to the O atom of the O_2^{2-} species, and the resulting OH fragment then binds to the CH_3 group to form CH_3OH. During the time period of our simulations (40~800 fs), the CH_3OH molecule would further desorb from the surface, thus confirming the direct formation of CH_3OH from CH_4 reaction with the O_2^{2-} species.

After CH_3OH desorption, hydrogen transfer from the H^+ species adsorbed at the O_t site to the OH^- species adsorbed at the La_t site readily occurs to form H_2O with a very low free energy barrier of 30.0 kJ mol^{-1}. Upon H_2O desorption, the stoichiometric La_2O_3(001) surface is regenerated. With the above catalytic cycle, the total reaction is $3CH_4$ (g) + O_2 (g) → $2CH_3$ (g) + CH_3OH (g) + H_2O (g), which is endothermic by 60.3 kJ mol^{-1} at 823 K. If the CH_3 radicals further combine to form C_2H_6, the total reaction becomes $3CH_4$ (g) + O_2 (g) → C_2H_6 (g) + CH_3OH (g) + H_2O (g), which is now exothermic by -141.2 kJ mol^{-1} at 823 K. The formation of C_2H_6 from two CH_3 radicals was calculated to be exothermic at -201.5 kJ mol^{-1} at 823 K. In addition, if further reaction of the resulting C_2H_6 always results in the formation of C_2H_4, whereas CH_3OH is completely oxidized by molecular O_2, the selectivity of C_2 products can be expected to be ~67%. However, the above must be considered as an ideal scenario, as many additional elementary reactions are likely to occur, some of which will be further discussed in the following section. Nevertheless, the direct oxidation of CH_4 by surface O_2^{2-} site suggests that this site should be responsible for CH_4 over-oxidation, which differs significantly from its role proposed by previous studies.[31]

CH_3OH Oxidation and CO_2 Formation.

As CH_3OH was not observed as one of the main products in the OCM reaction, we propose it to be an intermediate during CH_4 over-oxidation to CO_x (x = 1, 2). Further calculations show that CH_3OH can easily dissociate at the La_t-O_t pair site on the stoichiometric La_2O_3(001) surface to form the methoxy (CH_3O^-) and H^+ species adsorbed at the La_t and O_t sites with a relatively low free energy barrier of 68.0 kJ mol^{-1} at 823 K, as shown in Figure S8. The CH_3O^- species may be further oxidized to form CO_x. Karakaya et al. previously proposed a sequence of elementary steps for the OCM reaction over a La_2O_3/CeO_2 nanofabric catalyst,[44] where the CH_3O species was converted into CO by three dehydrogenation steps at the surface oxygen site via the formation of CH_2O and HCO intermediates. Energy barriers for CH_2O and HCO dehydrogenation were estimated to be only 55.0 and 6.8 kJ mol^{-1}, respectively, based on the Evans–Polanyi relationship[45] between reaction enthalpies and energy barriers, whereas CH_3O dehydrogenation was suggested to be barrierless due to its strong exothermicity. However, additional first principles calculations are necessary to verify the

possibility of the above pathway by calculating the energy barriers.

Contrary to the above proposed pathway for CH_3OH oxidation to CO, our calculations show that although CH_3OH can easily dissociate at the La_t–O_t pair site on the stoichiometric $La_2O_3(001)$ surface to form the CH_3O^- species at the La_t site (Figure S8), the CH_3O^- species cannot be further oxidized by the lattice O^{2-} site to form CO_x, as we failed to locate a local minimum with an H atom from the CH_3O^- species transferred to the neighboring O^{2-} site. This is consistent with the fact that the stoichiometric $La_2O_3(001)$ surface lacks oxidative capability, and its reaction with CH_4 or CH_3OH is best understood as an acid-base reaction.[34-36] Furthermore, direct desorption of the CH_3O radical from the $La_2O_3(001)$ surface from the CH_3OH chemisorption state is also unlikely to occur due to its very high endothermicity of 299.1 kJ mol^{-1} at 823 K. Thus, we propose that further oxidation of CH_3OH must occur by its reaction with the O_2^{2-} site, which may result from the above mechanism shown in Figure 2(a) or from direct O_2 dissociation.[23] We note that the coverage of surface O_2^{2-} sites resulting from this process may be limited due to the high endothermicity (202.2 kJ mol^{-1}) as well as the high free energy barrier (270.6 kJ mol^{-1}) for direct O_2 dissociation on the $La_2O_3(001)$ surface at 823 K, which is also a gas-surface reaction without pre-adsorption of the gaseous reactant. We note that the free energy barrier of O_2 dissociation is comparable to that of CH_4 activation on the clean La_2O_3 (001) surface, which suggests that the O_2 dissociation reaction is competitive with the CH_4 activation reaction. However, the O_2 partial pressure is generally much lower than that of CH_4 under realistic reaction conditions with typical inlet CH_4/O_2 volume ratios of 3~11,[19,44] which should result in a lower reaction rate for O_2 dissociation than that for CH_4 activation on the La_2O_3 (001) surface, according to the collision theory.[46] In fact, the local CH_4/O_2 volume ratio near the catalyst surface may be significantly higher, as much of the O_2 is already consumed in the early stages of the OCM reactor.[44] Thus, we consider the OCM reaction to be initiated by CH_4 activation rather than O_2 dissociation at the La–O pair site. Additionally, the process of O_2 activation involves a spin crossover as molecular O_2 has a triplet ground state, whereas surface O_2^{2-} species have a singlet ground state, so the reaction rate may be further limited.[47] However, it is difficult to predict to what extent the spin-crossover will affect the reaction rate of this process.. Nevertheless, we investigated the complete oxidation of CH_3OH by the O_2^{2-} site on the La_2O_3 (001) surface.

As shown in Figure 3, CH_3OH is oxidized by the surface O_2^{2-} site to form CO_2 in three separate steps. In the first step, oxidation of CH_3OH by the O_2^{2-} species to form $CH_2(OH)_2$ was predicted to be very exothermic at −175.7 kJ mol^{-1} with an modest free energy barrier of 124.7 kJ mol^{-1} at 823 K. Our calculations further show that CH_3OH adsorbs at the O_2^{2-} site on the $La_2O_3(001)$ surface with a sizable physisorption energy of −88.7 kJ mol^{-1} at 0 K, where the O atom from CH_3OH interacts with the La^{3+} site in a Lewis acid-base interaction at a La–O distance of 2.68 Å. Notably, CH_3OH physisorption at the La^{3+} site leads to significant change in the structure of the O_2^{2-} site in that the two O atoms from the O_2^{2-} site move toward the

subsurface. The distance between the bottom O atom from the O_2^{2-} site and the nearest La atom from the subsurface is reduced from 3.77 Å to 2.61 Å. Thus, CH_3OH oxidation by the O_2^{2-} site may differ significantly in nature from the other gas-surface reactions studied in this work at relatively low reaction temperature. Only one imaginary frequency (268i cm^{-1}) was predicted for the transition state, which also has the appropriate displacements. In addition, the alternative dehydrogenation reaction of CH_3OH at the O_2^{2-} site was also investigated. As shown in Figure S9, the hydrogen atom from the OH group can be transferred to the neighboring O_2^{2-} site, with the CH_3O^* species adsorbed at the bridge site between two La atoms. The free energy of this reaction is endothermic at 82.9 kJ mol^{-1} at 823 K, in contrast to the exothermic CH_3OH oxidation reaction to form $CH_2(OH)_2$, which indicates that the oxygen insertion mechanism for CH_3OH reaction at the O_2^{2-} site is favored over its dehydrogenation mechanism. Upon the desorption of $CH_2(OH)_2$, its direct dehydration in the gas phase can occur to form CH_2O, which was calculated to have a significant free energy barrier of 181.9 kJ mol^{-1} at 823 K, although with the assistance of an H_2O molecule, the free energy barrier was predicted to be much lower at 113.2 kJ mol^{-1}. Alternatively, we expect surface OH species to also accelerate the dehydration reaction of $CH_2(OH)_2$.

In the second step, CH_2O is oxidized by the O_2^{2-} site to form HCOOH, which is highly exothermic by −133.9 kJ mol^{-1} with an energy barrier of 158.2 kJ mol^{-1} at 823 K. The transition state was predicted to have only one imaginary frequency of 519i cm^{-1}. As shown in Figure S10, we also considered the dissociation of CH_2O at the O_2^{2-} site via the alternative hydrogen transfer mechanism, which leads to the formation of the CHO^* and OH^* adsorbates and the recovery of the lattice oxygen O^{2-} site. The resulting CHO^* species is adsorbed on the La_2O_3 surface with the C and O atoms bonded with the O^{2-} and La^{3+} sites, respectively. The free energy of this reaction was calculated to be highly exothermic by −212.9 kJ mol^{-1} at 823 K, and we were unable to locate its transition state, most likely due to the high exothermicity, consistent with an early transition state and a small (if any) energy barrier. After CHO^* formation, the remaining H atom can be further transferred to the neighboring OH^* adsorbate, leading to the formation of gaseous H_2O and CO. The free energy of this reaction step was calculated to be slightly endothermic at 13.0 kJ mol^{-1} at 823 K. Thus, CH_2O dehydrogenation at the O_2^{2-} site should result in the formation of CO in the OCM reaction, although further calculations are necessary to locate the relevant transition states, if present.

In the third step, HCOOH is oxidized by the O_2^{2-} site to form carbonic acid (H_2CO_3), which is exothermic by −271.1 kJ mol^{-1} with a free energy barrier of 165.3 kJ mol^{-1} at 823 K. The transition state has only one imaginary frequency of 374i cm^{-1}. Direct dehydration of H_2CO_3 in the gas phase to form CO_2 was calculated to have a free energy barrier of 166.8 kJ mol^{-1} at 823 K, although with the assistance of an H_2O molecule, the free energy barrier was predicted to be much lower at 104.2 kJ mol^{-1}. At 0 K, the direct gas phase dehydration of H_2CO_3 was predicted to be exothermic by −36.4 kJ mol^{-1} with an energy barrier of

171.5 kJ mol^{-1} at the CCSD(T)/complete basis set (CBS) theory level, whereas the effective energy barrier of the dehydration mediated by an additional H_2O molecule was calculated to be 74.1 kJ mol^{-1},[48] and our present B3LYP results of -4.5, 184.9, and 97.9 kJ mol^{-1}, respectively, are in line with the previously calculated more accurate CCSD(T) results. Again, we expect surface OH species to also accelerate the dehydration of H_2CO_3.
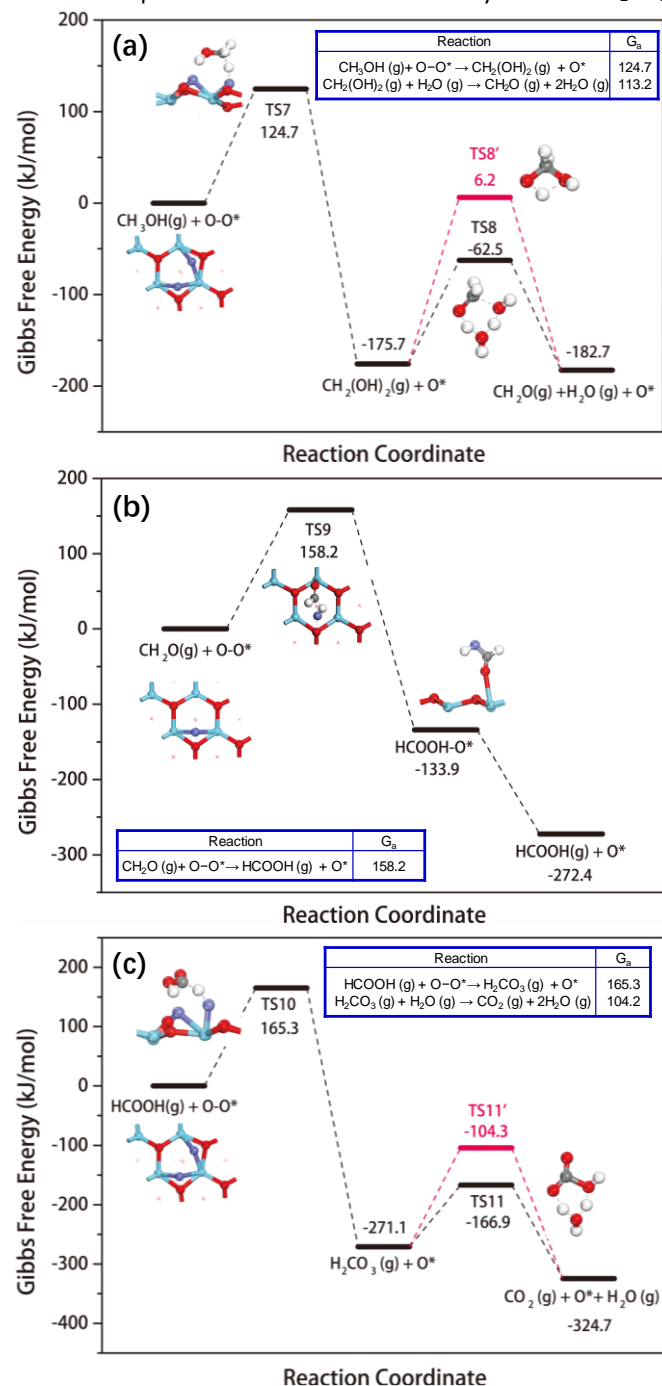
Figure 3. Calculated Gibbs free energy diagram(ΔG_{823K}, kJ mol^{-1}) for CH_3OH complete oxidation at the O_2^{2-} site on the La$_2$O$_3$(001) surface. (a) CH_3OH oxidation and CH_2O formation. (b) CH_2O oxidation and HCOOH formation. (c) HCOOH oxidation and CO_2 formation. Dehydration of $CH_2(OH)_2$ and H_2CO_3 can occur directly (red) or with the H_2O assistance (black).

In addition, we also investigated the alternative reaction pathway for the direct dehydration of HCOOH to form CO and H_2O. As shown in Figure S11, the free energy barrier and reaction energy for HCOOH direct dehydrogenation was calculated to be 286.0 kJ/mol and 19.4 kJ/mol, respectively, and with the assistance of an additional H_2O molecule, the free energy barrier was reduced be 230.7 kJ mol^{-1}. Thus, compared to the reaction pathway shown in Figure 3c for HCOOH oxidation by surface O_2^{2-} species to form H_2CO_3 and CO_2, direct dehydrogenation of HCOOH to form CO has a much higher free energy barrier, suggesting that in the presence of molecular O_2 and surface O_2^{2-} species, CO_2 formation is favored over CO formation.

Thus, our calculations show that the sequential oxidation of CH_3OH by the O_2^{2-} site involves modest energy barriers of no more than ~165 kJ mol^{-1}. Based on our predicted pathway for the complete oxidation of CH_4 on the La$_2$O$_3$(001) surface, the rate determining step (RDS) is the initial CH_4 oxidation step at the O_2^{2-} site with a significant free energy barrier of 236.8 kJ mol^{-1} at 823 K as shown in Figure 2(b). If the O_2^{2-} site is formed via direct O_2 dissociation on the La$_2$O$_3$(001) surface, then this step becomes the RDS with an even higher free energy barrier of 270.6 kJ mol^{-1} at 823 K. Thus, a relatively high reaction temperature is still required to reach an appreciable oxidation rate catalyzed by the La$_2$O$_3$(001) surface.

CH$_4$ Oxidation Reaction Network.

Based on our calculated free energy surfaces, we constructed a first principles-based reaction network for the evolution of the surface oxygen species and the formation of CH_3 radicals from CH_4 over the La$_2$O$_3$(001) surface. A possible mechanism for CO_2 formation was also proposed, although we note that the oxidation of CH_3 radicals in the gas phase may also occur at these relatively high temperatures.[49–51] As shown in Figure 4, our proposed reaction network includes twelve elementary steps (ES), two of which are gas phase reactions (ES8 for $CH_2(OH)_2$ dehydration and ES11 for H_2CO_3 dehydration). Furthermore, the formation of C_2H_6 from the coupling of two CH_3 radicals in the gas phase is a very exothermic reaction with no energy barrier, whereas the formation of C_2H_4 from C_2H_6 is a multistep process involving further surface reactions, as the direct loss of H_2 from C_2H_6 in the gas phase was predicted to have a very high energy barrier of 487.2 kJ mol^{-1} at 0 K at the CCSD(T)/CBS level.[52] The reaction energies as well as the energy barriers for these elementary steps are further listed in Table 1.

With our proposed reaction mechanism, CH_4 is first activated at the lattice oxygen site on the La$_2$O$_3$(001) surface, which is highly endothermic with a high energy barrier. Thus, the direct dissociation of CH_4 on the La$_2$O$_3$(001) surface is a slow step, and molecular O_2 facilitates CH_4 conversion by driving the reaction towards CH_3 radical desorption especially at relatively low reaction temperature. A surface superoxo species is then generated, which can directly convert CH_4 into another CH_3 radical. Although molecular O_2 can promote the formation of the CH_3 radical and benefit CH_4 conversion, the CH_3 radical in the gas phase may be further oxidized by excess molecular O_2 to

form by-products CO_x at relatively high temperature, resulting in the loss of C_2 selectivity. Furthermore, the exothermicity from the oxidation of the CH_3 radical in the gas phase can contribute to the increase of the surface temperature in the OCM reaction, which may further promote CH_4 dissociation on the La_2O_3 surface and CH_3 radical desorption, leading to accelerated CH_4 oxidation in the presence of an abundant amount of O_2 in the gas phase. At the relatively high reaction temperature of >823K, direct desorption of the CH_3 radical after CH_4 dissociation at the La^{3+}-O^{2-} pair site becomes favoured over the O_2-assisted CH_3 desorption pathway, and this is followed by O_2 adsorption and the similar evolution of the surface oxygen species in the presence of gaseous O_2. However, when gaseous O_2 is depleted, the OCM reaction may follow a distinct pathway possibly involving the formation of H_2, which is likely akin to the non-oxidative dehydrogenation of CH_4. Thus, our proposed OCM reaction mechanism is likely more suitable at low to modest O_2 conversion rate.

Table 1. Free Energy of Reaction (ΔG_r) and Free Energy Barrier (G_a) for the Elementary Steps Shown in Figure 4 (823 K in kJ mol^{-1}).

Steps	ΔG_r	G_a
ES1	259.3	269.2
ES2	−65.7	106.6
ES3	130.7	237.3
ES4	−68.2	26.6
ES5	−125.4	236.8
ES6	−70.4	30.0
ES7	−175.7	124.7
ES8	−7.0	113.2
ES9	−133.9	158.2
ES10	−271.1	165.3
ES11	−53.6	104.2
ES12 [a]	202.2	272.1

[a] Ref. 23.

Our proposed reaction mechanism agrees well with the experimental results of Karakaya *et al.*,[44] who made model-based interpretation of spatially resolved concentration and temperature profiles measured in a laboratory-scale packed-bed reactor over a La_2O_3/CeO_2 nanofabric catalyst. With a CH_4/O_2 ratio of 9 in the feed, the O_2 concentration was found to decrease rapidly due to CH_4 consumption when the gas mixture entered the catalyst bed. In addition, the C_2H_4 and C_2H_6 profiles rise more slowly than those of CO_2 and H_2O, indicating that CH_4 combustion occurs prior to the oxidative coupling and C_2 product formation. The combustion of CH_4 provides the heat required for the OCM reaction, as the latter occurs at much higher reaction temperatures (~1073 K). When CH_4 passes through the La_2O_3 catalyst, oxygen is mostly consumed in the early stage of the reactor accompanied by a rapid increase of catalyst bed temperature; the temperature then falls off in the middle to latter stages of the reactor. For the over-oxidation of CH_4, we propose a possible mechanism based on its initial oxidation to CH_3OH at the O_2^{2-} site, followed by subsequent oxidations to CH_2O and $HCOOH$ before CO_2 formation. Although direct experimental evidence to support our proposed over-oxidation mechanism is still lacking, we note that for the partial oxidation of CH_4 on the YSZ catalyst, CH_2O has been identified by experiments of *Zhu et al.* as the intermediate for CO formation, and traces of CH_2O and $HCOOH$ have been detected in the product streams along with CO and CO_2.[53] However, their further experiments suggest that the mechanism on the YSZ catalyst is quite different from our proposal for the La_2O_3 catalyst, where oxygen vacancies are involved and the Mars–van Krevelen mechanism is at work.[54]

With our proposed reaction network, the O_2^{2-} species is responsible for complete CH_4 oxidation, in contrast to the previously proposed role of this species.[31] Our proposal is based on the evidence from our calculations using both the slab and cluster models,[33] and is consistent with the superior oxidative capability of the peroxide species. CO_2 is generated in four C-H activation steps from CH_4 by atomic oxygen insertion. Due to the high energy barrier for CH_4 activation at the O_2^{2-} site to form CH_3OH as well as that for direct O_2 dissociation at the O^{2-} site to form the O_2^{2-} site, we suggest that CO_2 formation over the La_2O_3 surface mainly occurs at the relatively high temperature region in the early stage of the OCM reactor.

Based on our proposed reaction network, the formation of CH_3 radicals in the La_2O_3-catalyzed OCM reaction is mainly attributed to CH_4 activation at the O^{2-} site followed by O_2-assisted (direct) CH_3 desorption at relative low (high) reaction temperature of <823 K (> 823 K), and CH_4 activation at the resulting $O_2^{\bullet-}$ site, each with a substantial energy barrier. The regeneration of the catalyst dictates the further activation of CH_4 at the O_2^{2-} site, leading to the formation of CH_3OH as an intermediate on the path to complete CH_4 combustion. If CH_3OH is oxidized solely by surface O_2^{2-} sites from direct O_2 dissociation, and all of the CH_3 radicals produced are converted into C_2 products, C_2 selectivity will be ~67%. However, the actual reaction mechanism is likely to be more complex. On the one hand, CH_3OH or other intermediates in CH_4 combustion may consume the surface O_2^{2-} sites, which helps to complete the catalytic cycle without producing more CH_3OH and leads to higher C_2 selectivity. On the other hand, CH_3 radicals in the gas phase may further react with O_2 at relatively high temperatures, resulting in CH_4 combustion and the loss of C_2 selectivity. The further oxidation of C_2H_6 and C_2H_4 would also result in lower C_2 selectivity. Thus, it is still a great challenge to reliably predict C_2 selectivity in the OCM reaction, and further studies are necessary to reach a more quantitative prediction model of the OCM reaction.

Temperature Effects on the Rate Constants and Reaction Mechanisms
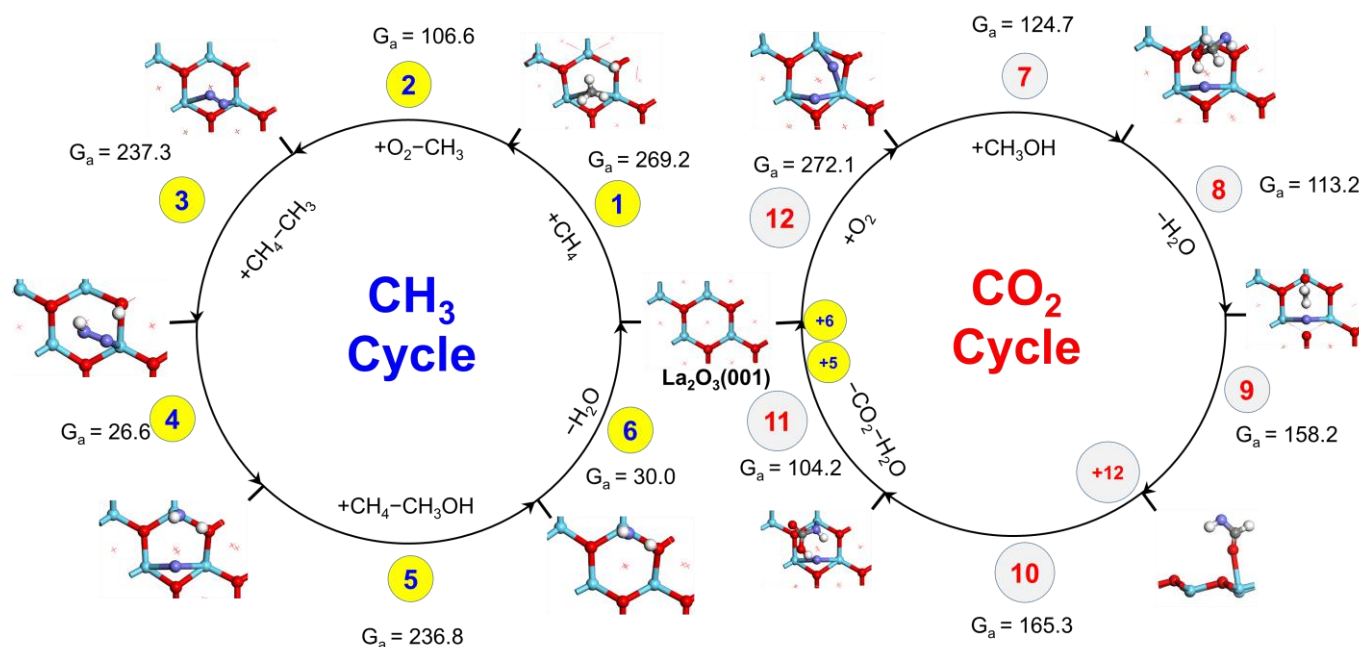
Figure 4. Proposed reaction network for selective (blue) and complete (red) CH_4 oxidation over the $La_2O_3(001)$ surface. Gibbs free energy barriers (G_a, 823 K, kJ mol^{-1}) for the elementary steps are also shown.

We have recently shown experimentally that the catalytic mechanism of the OCM reaction may be significantly influenced by the reaction temperature.[55] Although a detailed microkinetic model of the OCM reaction working at different temperatures is beyond the scope of the current work, we now qualitatively discuss temperature effects on the kinetics of the various elementary steps based on recent studies of model reactions such as methanol selective oxidation.[56] Based on the Arrhenius equation, the rate constant of an elementary step with an energy barrier depends on the exponential of the ratio of the classical activation energy and the reaction temperature and the pre-exponential factor. The latter is strongly influenced by the nature of the elementary step, and can be estimated by empirical rules,[56] although it can also be calculated from the thermodynamic formulation of the transition state theory with caution.

Thus, depending on the adsorption strength of the various adsorbates involved in the elementary steps, the elementary steps shown in Table 1 can be divided into three categories. The first category includes ES1, ES2, ES3, ES5, and ES12, which involves the reaction of a weakly adsorbed molecular species, CH_4 for ES1, ES3 and ES5, and O_2 for ES2 and ES12. Despite the known underestimation of the physisorption energies by the PBE functional, it is obvious that the molecular species involved in the above elementary steps are very weakly adsorbed on the

surface at 0 K, so at any relevant reaction temperature, these reactions should really be considered to occur by direct collisions of the gaseous reactants with the surface, which usually result in very low pre-exponential factors. Thus, these elementary steps are rather slow, especially those also involve high energy barrier at 0 K (E_a), i.e. ES1 (161.9 kJ mol^{-1}), ES3 (135.1 kJ mol^{-1}), ES5 (149.8 kJ mol^{-1}), and ES12 (121.3 kJ mol^{-1}). This explains the need for elevated temperature in the OCM reaction.

The second category includes ES7, ES9, and ES10, which are characterized by adsorbates of modest adsorption strength at 0 K, i.e. CH_3OH, CH_2O, and HCOOH. The two gas phase elementary steps (ES8 and ES11) may also be considered to fall into this group, as we expect that the dehydration of $CH_2(OH)_2$ and H_2CO_3 can also be catalyzed by the surface OH species, and these molecules should physisorb at the surface OH species with modest adsorption strength. At relatively low reaction temperature, physisorption of the above-mentioned molecules will occur, which is followed by surface-only reactions with usually high pre-exponential factors. In fact, the energy barrier at 0 K (E_a) of the surface-only reactions involved in elementary steps ES7, ES9, and ES10 are also modest at 90.8 kJ mol^{-1}, 94.6 kJ mol^{-1}, and 114.6 kJ mol^{-1}. At relatively high reaction temperatures, these elementary steps must again be considered to occur by direct collisions of the gaseous reactants

with the surface, although they all involve much lower energy bariers than those in the first category. Thus, the overall rate constants of the elementary steps in this category can be expected to be much greater than those in the first category.

The third category includes ES4 and ES6, which are purely surface reactions with strongly surface-bound species, so their pre-exponential factors should be much higher. In addition, the very low energy barrier at 0 K (E_a), 15.1 kJ mol^{-1} for ES4 and 22.2 kJ mol^{-1} for ES6, also make these elementary steps the fastest.

Therefore, the above discussion suggests that the RDS of the OCM reaction is likely one or more of the CH_4 and O_2 activation steps involved in ES1, ES3, ES5 and ES12. For the La_2O_3(001) surface, ES1 for CH_4 dissociation at the lattice oxygen site should be the slowest with its highest energy barrier at 0 K (E_a) of 161.9 kJ mol^{-1}. Nevertheless, this may not be true for the other low-index La_2O_3 surfaces, as the OCM reaction appears to be structure-sensitive, and our preliminary calculations on the reactivity of the La_2O_3 (011) surface show that ES1 for this surface involves a much lower energy barrier at 0 K of 72.4 kJ mol^{-1},[55] so the RDS for this surface can be expected to be different based on our present studies on the reaction network. Furthermore, more reliable identification of the preferable reaction pathway and the RDS in complex catalytic reactions requires detailed microkinetic simulations at realistic conditions using accurate energetics as demonstrated by recent large-scale computational simulations.[57,58] Our ongoing studies aim at revealing the possible elementary steps on other low-index La_2O_3 surfaces, as well as building a reliable microkinetic model based on our first principles studies on the OCM reaction.

Reliable experimental measurements of the activation energies and prefactors for the OCM reaction over the La_2O_3 catalyst are lacking, in part due to the often observed great difference between the oven temperature and catalyst bed temperature.[19] This has been largely resolved by the design of a novel reactor, and experimental apparent activation energies were obtained from the Arrhenius plots.[53] The experimental apparent activation energy of 341.6 kJ mol^{-1} deduced from the Arrhenius plots for C_2H_6 formation is significantly higher than the calculated energy barriers at 0 K in our reaction network. However, we found the above experimental value to match quite well with the calculated effective energy barrier at 0 K for CH_4 activation to directly form the CH_3 radical especially over the more reactive La_2O_3 (011) surface (354.1 kJ mol^{-1}), whereas this value was predicted to be 387.9 kJ mol^{-1} over the La_2O_3 (001) surface. Furthermore, our previous study identifies a "turn-over" zone in the temperature range of 853 K and 913 K, which is characterized by the rapid increase in the formation of C_2 products, the great decrease in the O_2 concentration, and the reduction in CO_x (x = 1, 2) formations, suggesting a change in the reaction mechanism.[55] This temperature range is close to the reaction temperature of 823 K investigated in this work, and our calculations show that above this temperature, direct CH_3 desorption is kinetically favoured over the O_2-assisted pathway, which may explain the change of the reaction mechanism. Nevertheless, more reliable kinetic measurements together with accurate microkinetic simulations of the OCM reaction

over the La_2O_3 catalyst are necessary to reach a more definitive conclusion.

Computational

Periodic DFT calculations were performed with the Perdew-Burke-Ernzerhof (PBE) exchange-correlation functional[59] and the projector-augmented wave (PAW) method.[60,61] The recommended default potentials were employed for all atoms, and an energy cutoff of 520 eV was used throughout this work. Spin polarization was applied, although it was found to have no effect on most of the systems studied in this work. Bulk La_2O_3 and its surfaces studied in this work all have significant band gaps, and Gaussian smearing with a width of 0.05 eV was applied. The electronic energy of the supercell was converged to 10^{-5} eV in the self-consistent field calculations, whereas the force on each relaxed atom was converged to 0.02 eV/Å in the ionic relaxation calculations.

A symmetric and stoichiometric slab model of the La_2O_3(001) surface was built from the optimized bulk structure, and the fractional coordinates are given in the Supporting Information. We have previously optimized the thickness of the La_2O_3 slab models by converging the O_2 dissociation energies to form surface O_2^{2-} sites to better than 0.01 eV.[23] For the La_2O_3(001) surface, the number of repeating units based on O_2 dissociation energy convergence with the p(1×1) unit cell was calculated to be two. Thus, two repeating units for the (001) surface along the surface normal were included in the slab models with the bottom half fixed at their bulk positions. A vacuum layer of 15 Å was inserted between adjacent slabs, and reactions were allowed only on the relaxed side of the slab. A p(2×2) supercell for the (001) surface was used with a Γ-centred Monkhorst-Pack k-point mesh of (3×3×1).

Dipole moment corrections along the surface normal should generally be applied for asymmetric slab models with adsorbates on only one side of the slab. For CH_4 physisorption and chemisorption structures on the La_2O_3 (001) surface, the sum of dipole and quadrupole energy corrections were calculated to be 2×10^{-3} eV and 3×10^{-3} eV, respectively, so the dipole effect on the potential energy surface is insignificant and dipole corrections were not included in further calculations.

Transition states were optimized with the climbing image nudged elastic band (CI-NEB) approach,[62,63] although the dimer method was also employed in some cases. Harmonic frequencies of the adsorbates in the local minima and transition states were calculated with a much tighter energy convergence of 10^{-8} eV, and zero-point energy (ZPE) corrections were included in the calculated energy barriers and reaction energies. The periodic DFT calculations were performed with VASP,[64,65] and the CI-NEB and dimer calculations were performed using the VASP transition state tools (VTST) interfaced with VASP with a much tighter energy convergence of 10^{-8} eV. The Atomic Simulation Environment (ASE) program was used to drive some of these calculations,[66] and the surface structures were built and visualized with Materials Visualizer from Materials Studio.[67] Electron localization function (ELF),[68–70] and crystal orbital

Hamilton population (COHP)[71,72] analyses were performed using VESTA[73] and lobster softwares,[74,75] respectively.

For CH_4 activation at the O_2^{2-} site, we further performed *ab initio* molecular dynamics (AIMD) simulations with VASP in the canonical ensemble employing Nosé‐Hoover thermostats[76,77] with a time step of 1 fs. Due to the limited time scale in the calculation, slow reaction processes may be precluded. Thus, a relatively high temperature of 1000 K was employed to explore the reactivity of the O_2^{2-} site.

The Gibbs free energy for each species in a given elementary step was calculated as $G = E_{elec} + E_{ZPE} - T*S$, where E_{elec} is the electronic energy at 0 K from the DFT calculation, and E_{ZPE} is the zero‐point energy term. For gaseous molecules, the entropic term calculated by the PBE functional using the VASPKIT program[78] is not sufficiently accurate as shown in Table S1, and we found that predictions from the B3LYP[79] hybrid exchange-correlation functional and the 6-31G* basis set[80-81] using the Gaussian 09 program package[82] are in much better agreement with the experimental values. For surface-adsorbed species, all 3N degrees of freedom of the adsorbate were treated as harmonic vibrations, and the entropy was calculated as a sum of the contributions from these vibrational motions. Although the above procedure may introduce some discrepancies for the calculations of entropies of gaseous and surface species, we note that the entropy of the gaseous species is significantly larger than that of the surface species due to the non-vibrational contributions, and thus can be expected to be more critical for the overall accuracy in the calculated energetics.

Conclusions

We systematically investigated CH_4 activation by different surface oxygen species (O^{2-}, $O_2^{\bullet-}$, and O_2^{2-}), and proposed a reaction network for the OCM reaction. The lattice oxygen site was found to activate CH_4 by heterolytic C−H bond splitting to yield the CH_3^- and H^+ fragments, which bind to the Lewis acid site (bridge La_b) and Brönsted base site (top O_t), respectively. Although the CH_3^- fragment binds quite strongly to the surface in the presence of the H^+ fragment, molecular O_2 can facilitate its desorption especially at relatively low reaction temperatures leading to the formation of an $O_2^{\bullet-}$ species. The $O_2^{\bullet-}$ species can further activate CH_4 by direct hydrogen abstraction, producing the second CH_3 radical. Comparing the free energy barriers of CH_3 radical formation at the O^{2-} and $O_2^{\bullet-}$ sites, we found the $O_2^{\bullet-}$ site to be kinetically favorable for selective conversion of CH_4 into the CH_3 radical. For CH_4 activation at the O_2^{2-} site, direct insertion of an O atom into the C−H bond leads to the formation of CH_3OH. However, CH_3OH is much less stable than CH_4 under the OCM conditions, and can be further oxidized by the O_2^{2-} site to form CO_2 in three C−H activation steps, whereas dehydrogenation of the CH_2O intermediate at this site can result in CO formation. Thus, our study suggests that surface O_2^{2-} species are responsible for CH_4 complete oxidation in the OCM reaction, where the first C−H bond activation is the rate−determining step. From our predicted pathway for CH_4 selective oxidation in the OCM reaction, C_2 selectivity is

predicted to be ~67% in the absence of competing reactions, although the selectivity could be significantly affected by side reactions. Our calculations provide important insights into the role of the surface oxygen species, as well as the reaction network for the selective and complete oxidation of CH_4 in the OCM reaction.

Conflicts of interest

There are no conflicts to declare.

Acknowledgements

Notes and references

1   M. C. Alvarez-Galvan, N. Mota, M. Ojeda, S. Rojas, R. M. Navarro and J. L. G. Fierro, *Catal. Today.* 2011, **171**, 15.
2   J. H. Lunsford, *Catal. Today.* 2000, **63**, 165.
3   J. S. Lee and S. T. Oyama, *Catal. Rev*. 1988, **30**, 249.
4   K. D. Campbell, E. Morales and J. H. Lunsford, *J. Am. Chem. Soc*. 1987, **109**, 7900.
5   P. Schwach, X. Pan and X. Bao, *Chem. Rev*. 2017, **117**, 8497.
6   H. Schwarz, *Angew. Chem. Int. Ed*. 2011, **50**, 10096.
7   U. Zavyalova, M. Holena, R. Schlögy and M. Baerns, *ChemCatChem.* 2011, **3**, 1935.
8   D. Driscoll, W. Martir, J. Wang and J. H. Lunsford, *J. Am. Chem. Soc*. 1985, **107**, 58.
9   T. Ito and J. H. Lunsford, *Nature.* 1985, **314**, 721.
10 M. Xu and J. H. Lunsford, *Catal. Lett*. 1911, **11**, 295.
11 S. Ji, T. Xiao, S. Li, C. Xu, R. Huo, K. S. Coleman and M. L. Green, *Appl. Catal. A* 2002 **225**, 271.
12 P. Wang, G. Zhao, Y. Wang and Y. Lu, *Sci. Adv*. 2017, **3**, e1603180.
13 P. Tang, Q. Zhu, Z. Wu and D. Ma, *Energy. Environ. Sci*. 2014, **7**, 2580.
14 K. Takanabe and E. Iglesia, *Angew. Chem. Int. Ed*. 2008, **47**, 7689.
15 K. D. Campbell, H. Zhang and J. H. Lunsford, *J. Phys. Chem*. 1988, **92**, 750.
16 J. M. DeBoy and R. F. Hicks, *Ind. Eng. Chem. Res*. 1988, **27**, 1577.
17 S. Kuś, M. Otremba and M. Taniewski, *Fuel* 2003, **82**, 1331.
18 D. Noon, A. Seubsai and S. Senkan, *ChemCatChem* 2013, **5**, 146.

19 T. Jiang, J. Song, M. Huo, N. Yang, J. Liu, J. Zhang, Y. Sun and Y. Zhu, *RSC. Adv.* 2016, **6**, 34872.
20 C. Hammond, S. Conrad and I. Hermans, *ChemSusChem.* 2012, **5**, 1668.
21 S. Lacombe, H. Zanthoff and C. Mirodatos, *J. Catal.* 1995, **155**, 106.
22 M. S. Palmer and M. Neurock, *J. Phys. Chem. B* 2002, **106**, 6543.
23 S. Wang, L. Cong, C. Zhao, Y. Li, Y. Pang, Y. Zhao, S. Li and Y. Sun, *Phys. Chem. Chem. Phys.* 2017, **19**, 26799.
24 J. H. Lunsford, *Angew. Chem. Int. Ed.* 1995, **34**, 970.
25 D. J. Discoll, W. Martir, J. Wang and J. H. Lunsford, *J. Am. Chem. Soc.* 1985, **107**, 58.
26 J. H. Lunsford, X. Yang, K. Haller, J. Laane, G. Mesti and H. Knoezinger, *J. Phys. Chem.* 1993, **97**, 13810.
27 D. Dissanayake, J. H. Lunsford and M. P. Rosynek, *J. Catal.* 1993, **143**, 286.
28 J. Wang and J. H. Lunsford, *J. Phys. Chem.* 1986, **90**, 3890.
29 C. Louis, T. L. Chang, M. Kermarec, T. Le Van, M. Tatibuët and M. Che, *Colloids. Surf. A: Physiochem. Eng. Aspects*. 1993, **72**, 217.
30 J. Xu, Y. Zhang, X. Xu, X. Fang, R. Xi, Y. Liu, R. Zheng, X. Wang, *ACS Catal.* 2019, **9**, 4030.
31 M. S. Palmer, M. Neurock and M. M. Olken, *J. Am. Chem. Soc.* 2002, **124**, 8452.
32 Z. Wang, D. Wang, and X. Gong, *ACS Catal.* 2020, **10**, 586.
33 C. Chu, Y. Zhao, S. Li and Y. Sun, *J. Phys. Chem. C* 2014, **118**, 27954.
34 C. Chrétien and H. Metiu, *J. Phys. Chem. C.* 2014, **118**, 27336.
35 Y. Lei, C. Chu, S. Li and Y. Sun, *J. Phys. Chem. C* 2014, **118**, 7932.
36 C. Chu, Y. Zhao, S. Li and Y. Sun, *Phys. Chem. Chem. Phys.* 2016, **18**, 16509.
37 P. Schwach, N. Hamilton, M. Eichelbaum, L. Thum, T. Lunkenbein, R. Schlögl and A. Trunschke, *J. Catal.* 2015, **329**, 574.
38 E. Sanville, S. D. Kenny, R. Smith and G. Henkelman, *J. Comp. Chem.* 2007, **28**, 899.
39 G. Henkelman, A. Arnaldsson and H. A Jónsson, *Comput. Mater. Sci.* 2006, **36**, 254.
40 W. Tang, E. Sanville and G. Henkelman, *J. Phys.: Condens. Matter.* 2009, **21**, 084204.
41 Y.-R. Luo, *Comprehensive Handbook of Chemical Bond Energies*, CRC Press, Taylor and Francis Group, Boca Raton, FL, USA, 2007.
42 K. Kwapien, J. Paier, J. Sauer, M. Geske, U. Zavyalova, M. Horn, P. Schwach, A. Trunschke and R. Schlögl, *Angew. Chem. Int. Ed.* 2014, **53**, 8774.
43 C. S. Cooper, R. J. Oldman and C. R. A. Catlow, *Chem. Commun.* 2015, **51**, 5856.
44 C. Karakaya, H. Zhu, B. Zohour, S. Senkan and R. J. Kee, *ChemCatChem.* 2017, **9**, 4538.
45 M. G. Evans and N. P. Polanyi, *Trans. Faraday Soc.* 1938, **34**, 11.
46 T. N. M, Le, B. Liu, and L. K. Huynh, *J. Comput. Chem.* 2014, **35**, 1890.
47 D. P. Solowey, M. V. Mane, T. Kurogi, P. J. Carroll, B. C. Manor, M.-H. Baik and D. J. Mindiola, *Nat. Chem.* 2017, **9**, 1126.
48 M. T. Nguyen, M. H. Matus, V. E. Jackson, V. T. Ngan, J. R. Rustad and D. A. Dixon, *J. Phys. Chem. A* 2008, **112**, 10386.
49 R. Zellner and F. Ewig, *J. Phys. Chem.* 1988, **92**, 2971.
50 R. Zhu, C.-C. Hsu and M. C. Lin, *J. Chem. Phys.* 2001, **115**, 195.
51 J. B. Burkholder, J. P. D. Abbatt, R. E. Huie, M. J. Kurylo, D. M. Wilmouth, S. P. Sander, J. R. Barker, C. E. Kolb, V. L. Orkin and P. H. Wine, Chemical Kinetics and Photochemical Data for Use in Atmospheric Studies: Evaluation Number 18; JPL Publication 15−10, National Aeronautics and Space Administration, Jet Propulsion Laboratory, California Institute of Technology: Pasadena, CA June 10, 2015.

52 M. T. Nguyen, V. S. Nguyen, M. H. Matus, G. Gopakumar and D. A. Dixon, *J. Phys. Chem. A* 2007, **111**, 679.
53 J. Zhu, J. G. van Ommen and L. Lefferts, *J. Catal.* 2004, **225**, 388
54 J. Zhu, J. G. van Ommen, H. J. M. Bouwmeester and L. Lefferts, *J. Catal.* 2005, **233**, 434
55 Z. Liu, J. P. H. Li, E. Vovk, Y. Zhu, S. Li, S. Wang, A. P. van Bavel and Y. Yang, *ACS Catal.* 2018, **8**, 11761.
56 C. Reece, E. A. Redekop, S. Karakalos, C. M. Friend and R. J. Madix, *Nat. Catal.* 2018, **1**, 852.
57 Z. W. Ulissi, A. J. Medford, T. Bligaard and J. K. Nørskov, *Nat. Commun.* 2017, **8**, 14621.
58 B. Wang, S. Chen, J. Zhang, S. Li and B. Yang, *J. Phys. Chem. C* 2019, **123**, 30389
59 J. P. Perdew, K. Burke and M. Ernzerhof, *Phys. Rev. Lett.* 1996, **77**, 3865.
60 P. E. Blöchl, *Phys. Rev. B* 1994, **50**, 17953.
61 G. Kresse and J. Joubert, *Phys. Rev. B* 1999, **59**, 1758.
62 G. Henkelman and H. Jónsson, *J. Chem. Phys.* 2000, **113**, 9901.
63 G. Henkelman and H. Jónsson, *J. Chem. Phys.* 2000, **113**, 9978.
64 G. Kresse and J. Furthmuller, *Comput. Mater. Sci.* 1996, **6**, 15.
65 G. Kresse and J. Furthmuller, *Phys. Rev. B.* 1996, **54**, 11169.
66 H. Larsen, *et al. J. Phys.: Condens. Matter.* 2017, **29** 273002
67 Materials Studio, Release 2018, Biovia Software Inc., 5005 Wateridge Vista Drive, San Diego, CA 92121 USA.
68 B. Silvi and A. Savin, *Nature.* 1994, **371**, 683.
69 A. Savin, R. Nesper, S. Wenger and T. F. Fassler, *Angew. Chem., Int. Ed.* 1997, **36**, 1808.
70 M. Kohout, F. R. Wagner and Y. Grin, *Theor. Chem. Acc.* 2002, **108**, 150.
71 R. Dronskowski and P. E. Blöchl, *J. Phys. Chem.* 1993, **97**, 8617−8624.
72 V. L. Deringer, A. L. Tchougréeff and R. Dronskowski, *J. Phys. Chem. A.* 2011, **115**, 5461.
73 K. Momma and F. Izumi, *J. Appl. Crystallogr.* 2011, **44**, 1272.
74 S. Maintz, V. L. Deringer, A. L. Tchougréeff and R. Dronskowski, *J. Comput. Chem.* 2013, **34**, 2557.
75 S. Maintz, V. L. Deringer, A. L. Tchougréeff and R. Dronskowski, *J. Comput. Chem.* 2016, **37**, 1030.
76 W. G. Hoover, *Phys. Rev. A* 1985, **31**, 1695.
77 S. J. Nosé, *Chem. Phys.* 1984, **81**, 511.
78 V. Wang and N. Xu, VASPKIT: A pre- and post-processing program for the VASP code. http://vaspkit.sourceforge.net.
79 A. D. Becke, *J. Chem. Phys.* 1993, **98**, 5648.
80 V. A. Rassolov, M. A. Ratner, J. A. Pople, P. C. Redfern and L. A. Curtiss, *J. Comput. Chem.* 2001, **22**, 976.
81 V. A. Rassolov, J. A. Pople, M. A. Ratner and T. L. Windus, *J. Chem. Phys.* 1998, **109**, 1223.
82 M. J. Frisch, G. W. Trucks, H. B. Schlegel, G. E. Scuseria, M. A. Robb, J. R. Cheeseman, G. Scalmani, V. Barone, B. Mennucci and G. A. Petersson, Gaussian 09, Revision C.01, Gaussian, Inc., Wallingford, CT, 2009.

Table of Contents
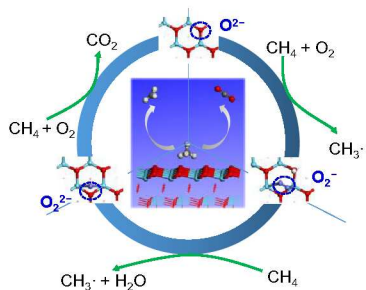
Catalytic mechanism and reaction network of oxidative coupling of methane over La_2O_3 is thoroughly investigated by density functional theory calculations.